JACS
JOURNAL OF THE AMERICAN CHEMICAL SOCIETY
Article
pubs.acs.org/JACS

NanoCOT: Low-Cost Nanostructured Electrode Containing Carbon, Oxygen, and Titanium for Efficient Oxygen Evolution Reaction

Zhichao Shan,[†,‡] Panikar Sathyaseelan Archana,[†,‡] Gang Shen,[∥] Arunava Gupta,[†,‡,§] Martin G. Bakker,[†] and Shanlin Pan*[,†,‡]

[†]Department of Chemistry, The University of Alabama, Tuscaloosa, Alabama 35487-0336, United States
[‡]Center for Materials for Information Technology, The University of Alabama, Tuscaloosa, Alabama 35487-0209, United States
[§]Department of Chemical and Biological Engineering, The University of Alabama, Tuscaloosa, Alabama 35487-0203, United States
[∥]Department of Electrical and Computer Engineering, The University of Alabama, Tuscaloosa, Alabama 35487-0200, United States

Supporting Information

ABSTRACT: Developing high-efficiency, durable, and low-cost catalysts based on earth-abundant elements for the oxygen evolution reaction (OER) is essential for renewable energy conversion and energy storage devices. In this study, we report a highly active nanostructured electrode, NanoCOT, which contains carbon, oxygen, and titanium, for efficient OER in alkaline solution. The NanoCOT electrode is synthesized from carbon transformation of TiO_2 in an atmosphere of methane, hydrogen, and nitrogen at a high temperature. The NanoCOT exhibits enhanced OER catalytic activity in alkaline solution, providing a current density of 1.33 mA/cm^2 at an overpotential of 0.42 V. This OER current density of a NanoCOT electrode is about 4 times higher than an oxidized Ir electrode and 15 times higher than a Pt electrode because of its nanostructured high surface area and favorable OER kinetics. The enhanced catalytic activity of NanoCOT is attributed to the presence of a continuous energy band of the titanium oxide electrode with predominantly reduced defect states of Ti (e.g., Ti^{1+}, Ti^{2+}, and Ti^{3+}) formed by chemical reduction with hydrogen and carbon. The OER performance of NanoCOT can also be further enhanced by decreasing its overpotential by 150 mV at a current density of 1.0 mA/cm^2 after coating its surface electrophoretically with 2.0 nm IrO_x nanoparticles.

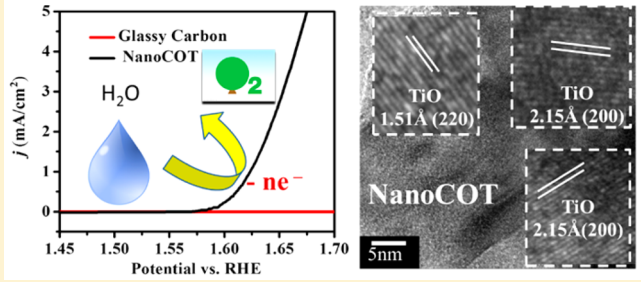

1. INTRODUCTION

The oxygen evolution reaction (OER, $2H_2O \rightarrow O_2 + 4H^+ + 4e^-$ in acid; $4OH^- \rightarrow O_2 + 2H_2O + 4e^-$ in alkaline solution) is one of the critical half-reactions of solar water splitting.[1] Efficient OER holds the promise for addressing the challenge of solar water splitting for large-scale storage of intermittent energy using hydrogen from the sun, wind, and other renewable sources.[2−10] However, one of the major obstacles to widespread adoption of water splitting is the low efficiency of the electrode materials and their high capital cost because of the use of noble metals. The OER involves sluggish kinetics at most electrodes, which has limited electrocatalysis being viable on an industrial scale.[11−14] Catalysts such as Ru, Ir, and Pt have shown desirable electrocatalytic activity; however, their scarcity and prohibitive cost renders their use impractical for large-scale applications.[15−20] Thus, it is important to develop inexpensive and highly active OER catalysts to overcome these obstacles. There has been an enormous amount of research efforts to investigate new earth-abundant materials containing Co, Ni, Mn, Fe, Mo, or graphene-based materials.[21−33] Among these materials, Fe- or Co-based catalysts have seen extensive efforts: for example, catalysts containing Co^{2+} in neutral aqueous phosphate solution[21] and the optimal intrinsic catalyst $Ba_{0.5}Sr_{0.5}Co_{0.8}Fe_{0.2}O_{3-\delta}$ (BSCF).[22] Nanostructured metal oxides such as MnO_x,[34] NiO_x,[31] or Co_3O_4 on graphene[23] and complex oxides such as $NiCo_2O_4$,[35] $CaMn_4O_x$,[13] $M_xFe_{3-x}O_4$ (M = Ni, Co, Mn, Fe, or Zn)[36] and mesoporous $Ni_xCo_{3-x}O_4$ nanowire[33] have been developed for enhancing OER efficiency. Improved understanding of the structure−function relationship of these catalytic electrode materials for OER and their large scale applications under harsh conditions have yet to be achieved.

Recently, our study showed that an anodized Ti electrode can be doped with carbon to form highly active nanostructured electrode materials for charge storage and other relevant redox reactions (e.g., electrogenerated chemiluminescence).[37] Here, we present the synthesis and characterization of such NanoCOT electrodes containing carbon, oxygen, and titanium for efficient OER and complete water splitting. The NanoCOT electrode is a low-cost electrode material and has a nanostructured surface with excellent activity for OER in alkaline solution. NanoCOT is synthesized by the facile carbon thermal transformation of nanostructured TiO_2 film or TiO_2 NPs in an

Received: May 23, 2015
Published: September 4, 2015

DOI: 10.1021/jacs.5b05367
J. Am. Chem. Soc. 2015, 137, 11996−12005

atmosphere of methane, hydrogen, and nitrogen. In comparison with semimetallic titanium oxycarbides synthesized by carbothermal reactions as reported previously in the literature,[38,39] the NanoCOT possesses enhanced OER reactivity that is comparable to oxidized Ir or Pt in alkaline solution and can be engineered to serve as a cathode or anode for complete water splitting.

2. EXPERIMENTAL SECTION

2.1. Materials. Titanium plate (Ti, 99%, 0.5 mm in thickness), titanium wire (Ti, 99.98%, 0.5 mm in diameter), sodium molybdate dihydrate ($Na_2MoO_4{\cdot}2H_2O$, 99%), tetrabasic sodium pyrophosphate ($Na_4P_2O_7$, 98%), sodium bicarbonate ($NaHCO_3$, 99%), potassium hexachloroiridate (IV) (K_2IrCl_6, Ir 39% min), iridium wire (99.8%, 0.5 mm in diameter), and platinum wire (Pt, 99.9%, 0.45 mm in diameter) were purchased from Alfa Aesar. Nickel(II) chloride hexahydrate ($NiCl_2{\cdot}6H_2O$, 97%), anhydrous zinc chloride ($ZnCl_2$, 99%), sodium sulfate (Na_2SO_4, 99%), sulfuric acid (H_2SO_4, ACS grade), hydrochloric acid (HCl, ACS grade), and methanol (CH_3OH, ACS grade) were purchased from Fisher Scientific. TiO_2 nanopowder (Aeroxide P25), iron(III) nitrate nonahydrate ($Fe(NO_3)_3{\cdot}9H_2O$, 98%), poly(methyl methacrylate) (PMMA; MW 15000), and hydrazine hydrate (N_2H_4, 64%) were purchased from Acros Organics. Hexaammineruthenium(III) chloride ($Ru(NH_3)_6Cl_3$, 98%) and Nafion solution (5% in ethanol) were purchased from Sigma-Aldrich. Poly(ethylene glycol)−poly(propylene glycol)−poly(ethylene glycol), or Pluronic P123, was purchased from BASF. Sodium hydroxide (KOH, ACS grade) was purchased from BDH. Gas mixture of 16% CH_4 and 20.51% H_2 balanced with N_2, 99.5% N_2, and 99.5% O_2 were purchased from Airgas. All reagents were used as received without further purification.

2.2. Fabrication of NanoCOT Electrode. As shown in Figure 1, NanoCOT electrode was fabricated by hydrothermal reaction of a Ti substrate to form Ti nanowires (NWs) on its surface, followed by air annealing and carbon transformation of the oxidized Ti NWs in a chemical vapor deposition (CVD) system.[40] Briefly, Ti plates were cleaned with ethanol and water prior to being loaded into a 45 mL Teflon-lined stainless steel autoclave containing 10 mL of 0.6 M HCl solution. The autoclave was heated at 190 °C for 12 h. After cooling to room temperature, the as-prepared Ti NW samples were annealed in air at 450 °C for 10 h to form the desired surface oxidized Ti NW substrates. The thermally annealed Ti NW substrates were then treated with 0.5 M $Fe(NO_3)_3$ for 20 min and dried in air. The Fe catalyst-coated substrates were horizontally placed into a quartz boat with a quartz plate cover on top to allow sufficient mixture gas retention time for the carbon transformation reaction. The boat was loaded in a tube furnace (1100, MTI Corporation, Richmond, CA). The chamber was purged by several vacuum/N_2 purge cycles to dispose of the oxygen in the furnace, followed by a constant N_2 gas flow. The furnace temperature was set to 900 °C with a ramp rate of 50 °C/min and a dwell time of 1 h. At ∼600 °C, the N_2 gas was turned off, and the $CH_4/H_2/N_2$ gas mixture was turned on at a flow rate of ∼1000 sccm and reduced to ∼100 sccm when the temperature reached 800 °C. After the carbon transformation reaction, the furnace was allowed to cool under $CH_4/H_2/N_2$ flow until the temperature of the furnace reached ∼600 °C. At this temperature, the $CH_4/H_2/N_2$ was turned off, and the N_2 flow was turned back on. The samples were allowed to cool to room temperature in a N_2 stream before being removed from the furnace.

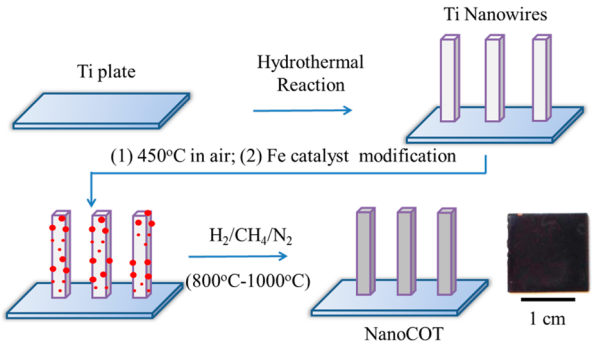

Figure 1. Schematic of preparation procedures for the NanoCOT electrode and a photograph of NanoCOT electrode (lower right inset) after carbon transformation of a nanostructured TiO_2 film.

2.3. Fabrication of Planar COT. Planar COT electrode fabrication followed the same procedure as for the NanoCOT electrode described above, except for using electropolished Ti substrates instead of nanostructured Ti NW substrates. The electropolished Ti substrates were obtained by anodizing a Ti substrates in a methanol solution containing 3 vol % sulfuric and 3 vol % hydrochloric acid at a current density of 0.1 mA/cm^2 at −40 °C.[41] The electropolished Ti substrates were then calcined at 550 °C for 10 h in air to form a thin layer of TiO_2. The TiO_2 layer was then converted to a COT electrode by following the same procedure outlined in section 2.2.

2.4. Synthesis of COT NPs. COT NPs were obtained by direct carbon transformation of TiO_2 NPs using the same CVD setup described above for both NanoCOT and planar COT samples; 100 mg P25, 20 mg P123, and 20 mg PMMA were then added to 30 mL of 3 mM $Fe(NO_3)_3$ acetone solution and stirred for 5 h at room temperature in a capped beaker. The resultant precipitate of Fe and surfactant-modified P25 were then centrifuged and dried prior to being grounded to a powder in a mortar. The obtained powder was placed horizontally in a quartz boat and heated at 450 °C in air for 1 h to remove the surfactant. N_2 gas was then used to purge the tube furnace to remove residual O_2 within the chamber prior to the carbon transformation process, as described in section 2.2.

2.5. Synthesis of NiMoZn/NanoCOT Cathode. NiMoZn alloy was electrodeposited onto a NanoCOT electrode by following the method reported by Nocera and co-workers.[42] Briefly, a solution of nickel(II) chloride hexahydrate (9.51 g L^{-1}), sodium molybdate dihydrate (4.84 g L^{-1}), anhydrous zinc chloride (0.0409 g L^{-1}), tetrabasic sodium pyrophosphate (34.57 g L^{-1}), and sodium bicarbonate (74.77 g L^{-1}) was used as an electrodeposition solution. Hydrazine hydrate (1.21 mL L^{-1}) was added immediately before plating. The NiMoZn alloy was deposited onto the NanoCOT electrode at a potential of −1.5 V vs Ag/AgCl for 20 min. The obtained electrodeposited film was then stored in 10 M KOH for 16 h to obtain suitable stoichiometry for enhanced proton reduction.

2.6. Electrophoretic Deposition of 2.0 nm IrO_x NPs onto NanoCOT Electrode. IrO_x particles (2.0 nm) were prepared and deposited onto NanoCOT by following the method reported by Murray and co-workers'.[43] Briefly, 2.4 mM aqueous K_2IrCl_6 at pH 13 was heated at 90 °C for 20 min and immediately cooled in an ice-bath, producing a blue 2.0 nm IrO_x nanoparticle solution. The 2.0 nm IrO_x particles were deposited by electrophoresis onto NanoCOT wire at 1.0 V vs Ag/AgCl.

2.7. Characterization. Surface morphology and chemical composition of the prepared catalysts were characterized using a JEOL 7000 field emission scanning electron microscope (FE-SEM). High-resolution transmission electron microscopy (HRTEM) images were recorded using a FEI Tecnai F-20 TEM. X-ray photoelectron spectroscopy (XPS) was performed using a Kratos XIS 165 system. X-ray diffraction patterns of samples were obtained using a Bruker D8 XRD system. A Nova 2200e surface area analyzer system was used to measure the Brunauer−Emmett−Teller (BET) surface area.

2.8. Electrochemical Characterization. The OER characterization of the NanoCOT, planar COT, or IrO_x-coated NanoCOT samples were measured in oxygen-saturated 0.1 M KOH in a three-electrode configuration using a CHI 760C potentiostat (CH Instruments, Austin, TX) at a scan rate of 5 mV/s. The electrochemical cell consisted of a catalytic electrode as the working electrode, a graphite rod counter electrode, and a Ag/AgCl reference electrode filled with saturated KCl solution. Polarization curves for water oxidation of COT samples were compared with indium tin oxide

DOI: 10.1021/jacs.5b05367
J. Am. Chem. Soc. 2015, 137, 11996−12005

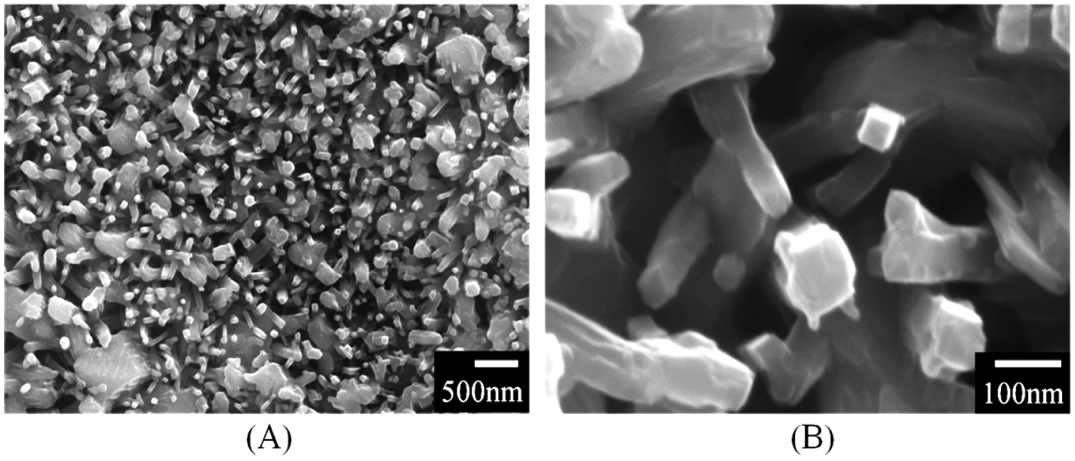

Figure 2. Low-resolution (A) and a zoom-in (B) SEM images of a NanoCOT electrode surface prepared by hydrothermal reaction of 1 × 1 cm^2 Ti plate (0.5 mm in thickness) followed by carbon transformation at 900 °C.

(ITO, <20 Ω/sq on polished soda lime float glass), IrO_2 (obtained by thermally annealing an Ir wire in air at 700 °C for 12 h), and Pt wire electrodes. Water electrolysis experiments were carried out in a two-electrode system with paired electrodes of NanoCOT, IrO_2, Pt, and NiMoZn/NanoCOT. The electrodes were placed 1.6 cm apart, and the electrode potential was scanned at 5 mV/s. The electrochemical performance of NanoCOT electrodes was also characterized in 1.0 M Na_2SO_4 containing 5.0 mM $Ru(NH_3)_6Cl_3$. Electrochemical impedance spectra (EIS) of samples were measured at 1.664 V (vs RHE) in the frequency range of 0.1−10000 Hz with an amplitude of 10 mV in 0.1 M KOH electrolyte. ZsimpWin (Princeton Applied Research) was used for fitting the experimental EIS data. The OER activities of COT NPs catalysts were measured using a rotating disc electrode (RDE) system (RRDE-3A, ALS, Co., Ltd., Tokyo, Japan) in a three-electrode cell. A Ag/AgCl electrode with saturated KCl was used as the reference electrode, and a glassy carbon disk (3 mm diameter) and Pt wire were used as the working and counter electrodes, respectively. In the RDE system, the working electrode was prepared by loading COT NPs (0.1 mg/cm^2; an ink mixture of 5 mg of COT NPs, 3 μL of Nafion solution, and 1 mL of ethanol) on the glassy carbon electrode. RDE measurements were conducted in an oxygen-saturated 0.1 M KOH solution (pH 13) at 25 °C using a scan rate of 10 mV/s. A solar cell panel for the complete water splitting test was assembled using 1.8 W Si solar cell modules with a size of 15 cm × 8 cm. Their average current and voltage output are 3.6 A and 0.5 V, respectively. A potentiometer was wired to these solar cell modules to control voltage output for complete water splitting with NanoCOT electrodes.

3. RESULTS AND DISCUSSION

3.1. Characterization of NanoCOT. The lower inset of Figure 1 shows a photograph of the NanoCOT electrode formed directly on a Ti plate. Color changes of a Ti substrate before and after the hydrothermal reaction and carbon transformation are shown in Figure S1 along with a photograph of a NanoCOT wire sample. Figure 2 shows the top-view SEM images of NanoCOT NWs after the carbon transformation reaction at 900 °C. The NW shape is already formed during the hydrothermal reaction of Ti substrate prior to forming NanoCOT, as shown in Figure S2 and detailed in our recent report.[44] The NW shape is retained after CVD treatment at 900 °C. Carbon nanotubes with diameters around 80 nm are formed at a temperature of 1000 °C (Figure S2). It is also observed that the Ti NWs melts at a temperature higher than 900 °C in air and that this melting process can be minimized in the presence of hydrogen and carbon from methane decomposition because of the formation of C-modified Ti_xO_y, which has a higher melting temperature than pristine TiO_2-coated Ti NWs.

Raman spectra in the range of 300−2000 cm^{-1} of the as-synthesized Ti NWs after thermal treatment and NanoCOT formation were recorded for investigation of TiO_2 and carbonaceous species formation (Figure 3). Raman features

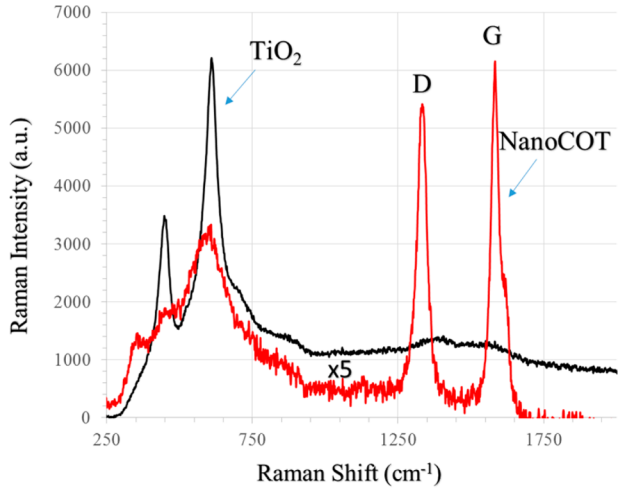

Figure 3. Raman spectra of NanoCOT electrode and TiO_2 NW electrode. The TiO_2 NW electrode was formed on a 1 × 1 cm^2 Ti substrate (0.5 mm in thickness) via hydrothermal reaction, followed by thermal annealing in air.

from 300 to 700 cm^{-1} are indicative of the formation of a TiO_2 shell on the Ti NWs.[44] These Raman features are weakened after the formation of NanoCOT because of chemical reduction and dramatic changes in the electronic structure TiO_2. After carbon transformation, the main Raman lines corresponding to the D and G bands of carbon can be detected. This implies that there is still a trace amount of carbon precipitates on the NanoCOT substrate during thermal annealing in methane and hydrogen.

The XRD image in Figure 4 shows that NanoCOT is isostructural with TiO (PDF card: 01-086-2352) and that there is an additional phase corresponding to reduced Ti oxide, such as Ti_2O_3 (PDF card: 00-043-1033), Ti_2O (PDF vard: 00-011-0218), and carbon (PDF card: 00-013-0148). As labeled in the figure, the peaks around 36.2°, 42°, 61°, 73°, and 76.9°,

DOI: 10.1021/jacs.5b05367
J. Am. Chem. Soc. 2015, 137, 11996−12005

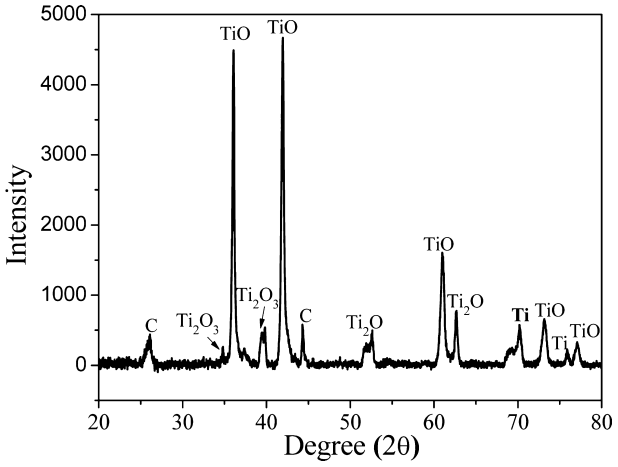

Figure 4. XRD spectrum of a NanoCOT electrode synthesized using carbon transformation method at 900 °C in a $CH_4/H_2/N_2$ atmosphere.

correspond to (111), (200), (220), (311), and (222) phases of TiO, respectively. We also took the XRD spectrum for planar COT and found that all peaks resembled the features of NanoCOT, as shown in Figure S3. The XRD pattern of planar COT was obtained with a Bruker D2.

Further insights into the effect of carbon transformation on the morphology and structure were obtained by HRTEM observations, as shown in Figure 5. A representative HRTEM image of thermally oxidized Ti NW, shown in Figure 5A, revealed lattice fringes of 2.99 and 3.26 Å, matching well with the *d*-spacing of ⟨001⟩ and ⟨110⟩ planes of rutile TiO_2. The selected area electron diffraction pattern in the upper left inset (Figure 5 A) further confirmed the single crystalline nature of the rutile TiO_2. After carbon transformation, HRTEM images of NanoCOT (Figure 5B, C, and D) showed polycrystalline titanium oxide in a reduced state. The close examinations at the NanoCOT revealed lattice fringes of 1.51 and 2.15 Å, corresponding to the (220) and (200) planes of TiO; 2.4 Å, corresponding to the (002) plane of Ti_2O; 2.19 Å, corresponding to the (111) plane of TiO_2; and a large amount of amorphous structure possibly attributed to a mixture of C, O, and Ti, in good agreement with the XRD analysis.

The chemical states of Ti, O, and C in NanoCOT were investigated by high-resolution XPS analysis (Figure 6). Before data acquisition, samples were sputtered by an Ar ion beam with incident energy of 3 keV for 30 s to clean the surface. Compared with the spectra of TiO_2, there are four doublet peaks corresponding to the four chemical states of Ti; namely, Ti^{1+}/Ti_2O (Ti $2p_{3/2}$, 455.1 eV; Ti $2p_{1/2}$, 461 eV), Ti^{2+}/TiO (Ti $2p_{3/2}$, 455.6 eV; Ti $2p_{1/2}$, 461.4 eV), Ti^{3+}/Ti_2O_3 (Ti $2p_{3/2}$, 456.8 eV; Ti $2p_{1/2}$, 462.7 eV), and Ti^{4+}/TiO_2 (Ti $2p_{3/2}$, 458.7 eV; Ti $2p_{1/2}$, 464.3 eV). The calculation of Ti atomic percentage base on the XPS spectra shows that the percentage of Ti^{1+}, Ti^{2+}, Ti^{3+}, and Ti^{4+} are 9%, 21%, 34% and 36%, respectively. The intense O 1s peak at 530.4 eV in Figure 6 B can be attributed to the O^{2-} anions of the Ti−O bond. Another relatively weaker peak at 532.1 eV is assigned to carbonate-like species to link with C 1s peaks rather than weakly absorbed species. The spectra for core level C 1s are shown in Figure 6 C. The major peak at 284.6 eV is assigned to the external

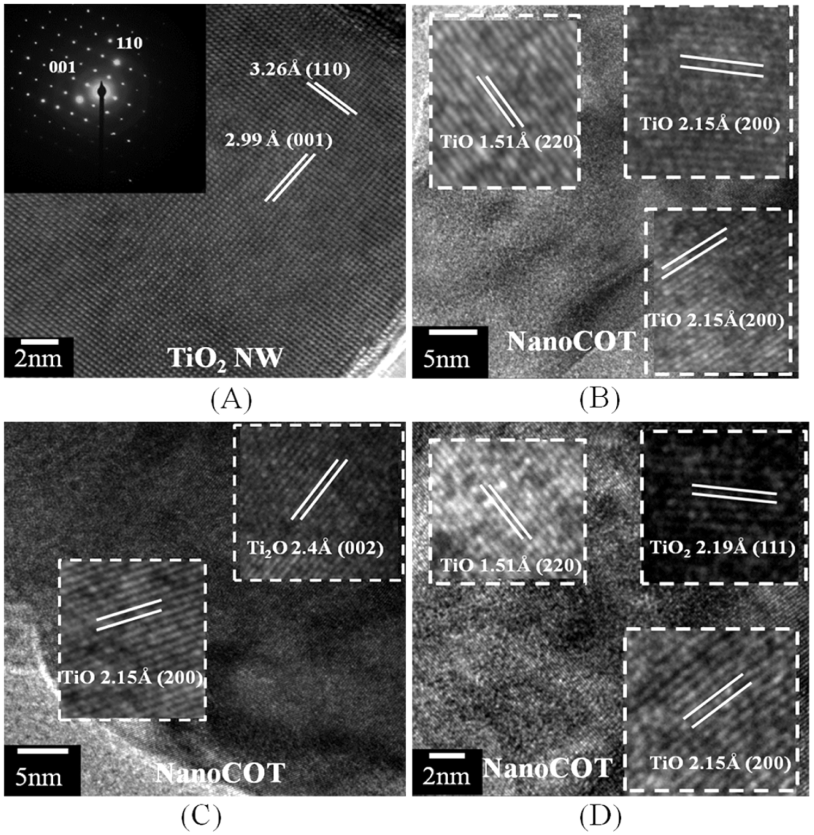

Figure 5. HRTEM images and electron diffraction patterns of oxidized Ti NWs (A) prior to the formation of NanoCOT and HRTEM images of selected regions of a NanoCOT electrode (B, C, D).

DOI: 10.1021/jacs.5b05367
J. Am. Chem. Soc. 2015, 137, 11996−12005

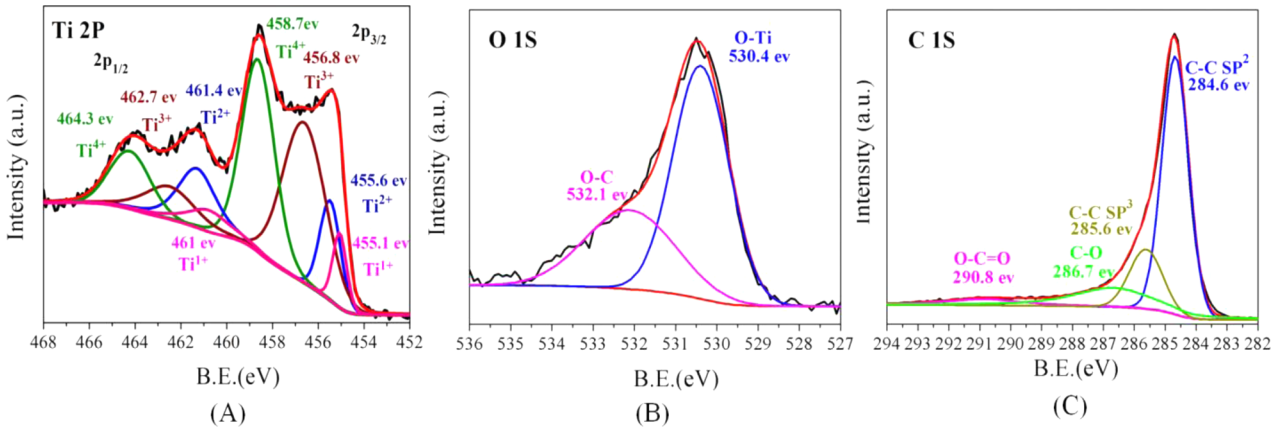

Figure 6. XPS analysis of titanium (A), oxygen (B) and carbon (C) in the NanoCOT electrode.

graphitic-like C−C sp^2 bond, and the peak at 285.6 eV is attributed to the diamond C−C sp^3 bond, as evidenced in the Raman analysis (cf. Figure 3). The peaks at ∼286.7 and 290.8 eV are ascribed to C−O and O−C═O bonds, respectively, whose concurrent presence indicates the formation of a Ti−O−C bond as a result of interstitial carbon in the TiO_{2-x} phase. Moreover, the composition results obtained from the XPS analysis also suggest that the empirical formula of NanoCOT can be estimated to be $TiO_{1.3}/C_{0.3}$.

The electrochemical activities of the obtained NanoCOT electrode were studied by using dynamic control of the electrode potential in the presence of a standard redox couple of $Ru(NH_3)_6^{2+}/Ru(NH_3)_6^{3+}$ and compared with the performance of other control electrodes, including a bare Ti electrode, Pt, and IrO_2 wire electrode. As shown in Figure 7, highly

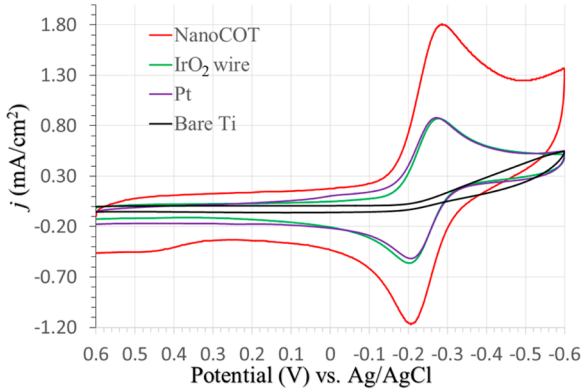

Figure 7. CVs of NanoCOT, Pt, IrO_2 wire, and a bare Ti electrode in 1.0 M Na_2SO_4 containing 5.0 mM $Ru(NH_3)_6Cl_3$ at a scan rate of 100 mV/s.

reversible cyclic voltammetries (CVs) of $Ru(NH_3)_6^{3+}$ can be obtained at the NanoCOT electrode with an ΔE of around 65 mV, which is close to that of the Pt or IrO_2 electrode. The ΔE that is slightly higher than the theoretical value of 2.3RT/nF (or 59 mV at 25 °C for $Ru(NH_3)_6^{3+} + e^- \rightarrow Ru(NH_3)_6^{2+}$) is due to the concentration overpotential at the large surface area (0.5 cm × 1 cm) of a NanoCOT electrode for the CV measurement. The NanoCOT electrode has ∼2-fold higher faradic current density than Pt or IrO_2 wire electrode as a result of the larger specific surface area of NanoCOT. This is consistent with the increase in its double layer charging current in the potential region from 0 to 0.4 V (vs Ag/AgCl).

3.2. Water Oxidation Performance. The polarization curves in Figure 8A for OER indicate that the anodic current per geometric surface area at NanoCOT (for both 1 × 1 cm^2 plate and 0.5 mm diameter wire samples) is much more active than ITO, IrO_2, and Pt wires. The thermodynamic potential of the OER half reaction in alkaline solution, $4OH^- \rightarrow O_2 + 2H_2O + 2e^-$, is given by $E = -0.401$ V + 0.059 pOH or 1.23 V − 0.059 pH vs normal hydrogen electrode (NHE). For reasons of convenience, all measured electrode potentials are converted to be relative to RHE using formula E (vs RHE) = E (vs NHE) + 0.059 pH. The log current density for all control electrodes are plotted against the overpotential (η) for OER as shown by Tafel plots in Figure 8B. Appreciable catalytic current is observed beginning at $\eta = 0.3$ for NanoCOT, which is the same as the IrO_2 wire and lower than the Pt wire (Figure 8B). All Tafel plots were fitted using a linear function, and their slopes and intercepts are listed in Table 1 along with the current density at $\eta = 0.42$. NanoCOT prepared on Ti wire generates a current density of 1.18 mA/cm^2 at $\eta = 0.42$, which is ∼4 times as high as the 0.32 mA/cm^2 for the IrO_2 wire and 15 times as high as the 0.08 mA/cm^2 for the Pt wire. Moreover, the OER efficiency of a planar COT electrode obtained from an electropolished Ti substrate, which was not treated to form Ti NW, is also comparable with IrO_2 wire. All slopes obtained are comparable because the slope is a function of $(1 - \alpha)F/2.3RT$, where α is the transfer coefficient for oxygen reduction reaction. The applied overpotential in the data-fitting region was not high enough for the ITO electrode to show reasonable OER activity, as shown in Figure 8A. The exchange current density values obtained from data fitting are consistent with the current density at $\eta = 0.42$ V, indicating favorable catalytic OER at the NanoCOT surface.

To optimize the OER performance, we also investigated the impact of the CVD temperature on the water oxidation reaction in 0.1 M KOH, as shown in Figure S4. The current density of the NanoCOT plate obtained from 800 °C carbon transformation is as low as 10 mA/cm^2 at 2 V vs RHE. The maximum activity is observed for the electrode treated in CVD at 900 °C, which achieved a current density of 25 mA/cm^2. A temperature above 900 °C leads to a decreased current density as a result of a greater carbon accumulation and carbon nanotubes formed on the NanoCOT surface, which block the active surface of NanoCOT from interacting with redox species. Thus, the ideal temperature for optimal carbon transformation is kept at 900 °C to achieve optimal OER performance. In addition to high activity, long-term stability is another critical

DOI: 10.1021/jacs.5b05367
J. Am. Chem. Soc. 2015, 137, 11996−12005

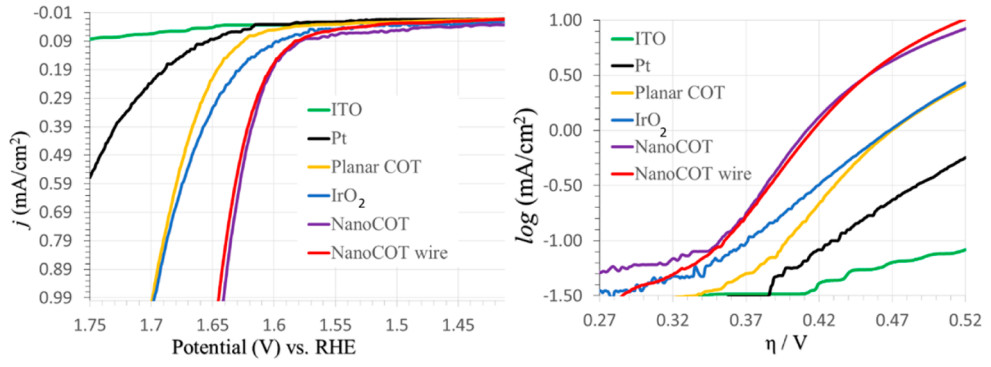

(A) (B)

Figure 8. (A) Polarization curves of a bare ITO, a NanoCOT (on 1 × 1 cm^2 Ti substrate), a NanoCOT prepared on 0.5 mm (in diameter) Ti wire, a planar COT obtained on electropolished Ti substrate, IrO_2 wire, and Pt wire electrodes (0.45 mm in diameter) in 0.1 M KOH solution for OER. Scan rate: 5 mV/s. Reference electrode: Ag/AgCl. Electrode potential is corrected to be relative to RHE using formula E (vs RHE) = E(vs Ag/AgCl) + 0.197 V + 0.059 pH. (B) Tafel plots for anodic branches of the log current density (mA/cm^2) vs overpotential (η) for OER reaction obtained under the same conditions as panel A. η = applied potential (vs RHE) − 1.23 V. Tafel plots are fitted in the region of η = 0.42−0.52 using a linear function to obtain their slope and intercept (or exchange current density, j_0), as listed in Table 1.

Table 1. Current Density at η = 0.42 V, Slope and Exchange Current Density j_0 for OER of NanoCOT[a], NanoCOT on Ti Wire, Planar COT, 0.5 mm Diameter IrO_2, and 0.45 mm Diameter Pt Wire Electrodes

electrode	j (mA/cm^2) at η = 0.42 V	slope, log(A/cm^2)/V	j_0, A/cm^2
NanoCOT on 0.5 mm Ti wire	1.18	9.2	2.0×10^{-7}
NanoCOT on 1 × 1 cm^2 Ti plate	1.33	7.7	9.3×10^{-7}
planar COT	0.22	10.6	1.0×10^{-8}
IrO_2 wire (0.5 mm)	0.32	9.3	4.5×10^{-8}
Pt wire (0.45 mm)	0.08	8.4	2.6×10^{-8}
planar ITO	0.04		

[a]On 0.5 mm diameter Ti wire and 1 × 1 cm^2 Ti plate. Results are obtained from Figure 8.

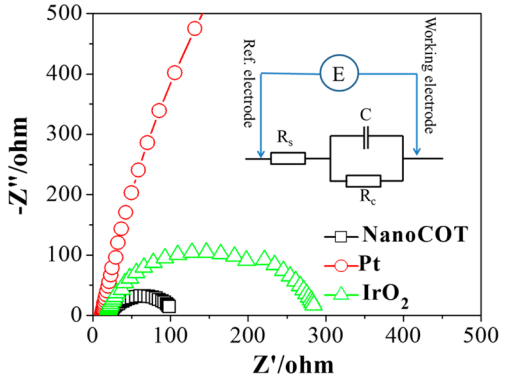

Figure 9. Nyquist plots of NanoCOT, IrO_2, and Pt wire samples at 1.664 V (vs RHE). Inset is the equivalent circuit used to fit the experimental data. Fitting results are shown in Table 2.

Table 2. AC Impedance Parameters Obtained by Fitting the Experimental Data in Figure 13

impedance	NanoCOT	IrO_2	Pt
R_s (Ω)	20	19	13
R_c (Ω)	71	243	3600
C (μF)	180	26	14

factor to determine the applicability of an OER electrode. The water splitting capability and stability of a NanoCOT electrode was tested in 0.1 M KOH when biased at 1.8 V against a Pt wire cathode. As shown in Figure S5, the current density remains around 5.5 mA/cm^2 after 17 h, and no apparent morphology change was observed after the electrolysis experiment, as shown by an SEM image of the sample (Figure S6).

3.3. AC Impedance. To elucidate the OER kinetics and charge transfer process and to obtain more quantitative information about the electrodes, AC impedance spectroscopy (EIS) was performed. Figure 9 shows typical Nyquist plots of the NanoCOT, IrO_2, and Pt electrodes at 1.664 V (vs RHE). All impedance spectra are fitted using an equivalent RC circuit model, as shown as inset of Figure 9, which consists of a resistor (R_s), representing the resistivity of the electrolyte between the working and reference electrodes; a charge transfer resistance (R_c), representing the charge transfer resistivity of the redox reaction; and a capacitance (C) in parallel with the (R), analogous to the double layer charging capacity of the solid−liquid junction. All fitting results are summarized in Table 2. No major differences in R_s of three different electrodes were found. The R_c of NanoCOT is 71 Ω, which is much lower than that found for wire electrodes of IrO_2 (243 Ω) and Pt (3600 Ω). This means that NanoCOT is more kinetically favorable than IrO_2 and Pt electrodes for OER. Pt shows poor OER activity because of the formation of an oxide layer, as shown by the increase in its R_c. Moreover, the capacitance is greatly enhanced for NanoCOT because of its high surface area.

3.4. Characterization and Electrochemical Catalytic Performance of COT NPs. The previously discussed NanoCOT samples are prepared on a planar or hydrothermally treated Ti substrate, and the top NanoCOT layer is naturally grown onto the Ti substrate for electrochemical testing and device fabrication (e.g., electrolyzer and solar cell). COT NPs are highly desirable for many other applications because of their high surface areas, allowing formation of electrode materials on other substrates, such as flexible transparent electrodes. Figure 10A shows the morphology of COT NPs. Figure S7 shows photographs of TiO_2 NPs before and after carbon transformation toward COT NPs. After carbon treatment at 900 °C, the big particles are mostly agglomerated, and the BET surface area is found to be 2.3 m^2/g (Figure S8). Figure 10B shows the

DOI: 10.1021/jacs.5b05367
J. Am. Chem. Soc. 2015, 137, 11996−12005

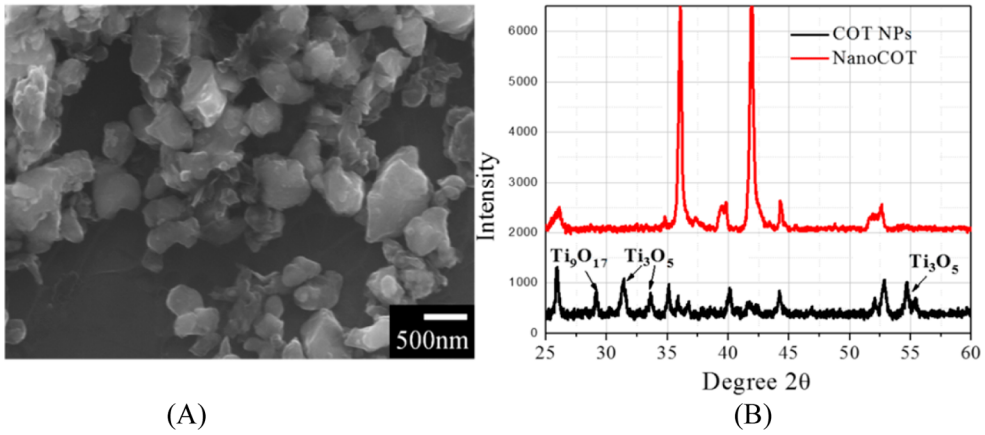

Figure 10. Typical SEM image of COT NPs obtained from TiO_2 NPs (A) and their XRD spectrum (B) in comparison with XRD of NanoCOT.

XRD pattern of the COT NPs catalyst. The XRD pattern is similar to NanoCOT, but shows poor crystallinity with lower amounts of Ti_2O, TiO,and Ti_2O_3 phases. Five new peaks around 29°, 31°, 33°, 54°, and 55° are observed, which can be attributed to the formation of other reduced titanium oxide phases, such as Ti_9O_{17} (PDF card: 01-085-1061) and Ti_3O_5 (PDF card: 04-008-6988), respectively.

The chemical states of O, Ti, and C in COT NPs were also investigated by XPS. The chemical composition of COT NPs was quite similar to NanoCOT. As shown in Figure S9, there are also four doublet peaks corresponding to the four chemical states of Ti; namely, Ti^{1+}/Ti_2O (Ti $2p_{3/2}$, 455.2 eV; Ti $2p_{1/2}$, 461.4 eV), Ti^{2+}/TiO (Ti $2p_{3/2}$, 456.2 eV; Ti $2p_{1/2}$, 462.3 eV), Ti^{3+}/Ti_2O_3 (Ti $2p_{3/2}$, 457.7 eV; Ti $2p_{1/2}$, 463.6 eV), and Ti^{4+}/TiO_2 (Ti $2p_{3/2}$, 459.3 eV; Ti $2p_{1/2}$, 465.2 eV). However, compared with the NanoCOT, the COT NPs have a lower amount of Ti^{1+}, Ti^{2+}, and Ti^{3+} and a higher amount of Ti^{4+}, which is in a good agreement with the COT NPs' XRD.

The calculation of Ti atomic percentage based on the COT NPs' XPS shows that the percentage of Ti^{1+}, Ti^{2+}, Ti^{3+}, and Ti^{4+} are 3%, 5%, 25%, and 67%, respectively. The intense O 1s peak at 530.7 eV in Figure S9B can be attributed to the O^{2-} anions of the Ti−O bond. Another relatively weaker peak at 531.8 eV can be assigned to the C−O bond. The results show a similar C−O content in COT NPs compared with NanoCOT with about one-third of the O atoms being bonded with C. The spectra for core level C 1s are shown in Figure S2. The major peak at 284.6 eV is assigned to the external graphitic-like C−C sp^2 bond, and the peak at 285.4 eV is attributed to the diamond C−C sp^3 bond. The peaks at ∼286.6 and 290.2 eV are associated with C−O and O−C═O bonds, respectively. On the basis of the XPS analysis results, the chemical formula of COT NPs is estimated to be $TiO_{1.9}/C_{0.3}$.

Figure 11 shows the OER catalytic characteristics recorded on glass carbon electrodes loaded with the COT NPs. As shown in the figure, the OER onset potential of the COT NPs is around 1.53 V (vs RHE) and generates a current density of 10 mA/cm^2 at a potential of 1.72 V (vs RHE), which is superior or comparable to nanostructured IrO_2 and other OER nano catalysts reported in the literature, such as Co_3O_4,[23] anodized Ni,[28] layered double hydroxide of Zn and Co,[30] $Mn_3O_4/CoSe_2$,[32] or Co/Mn/O,[45] depending on the surface area. The average OER performances of COT NPs, NanoCOT, IrO_2, and planar COT at 1.77 V vs RHE are shown in Figure 12. COT NPs shows the highest OER current density due to the surface

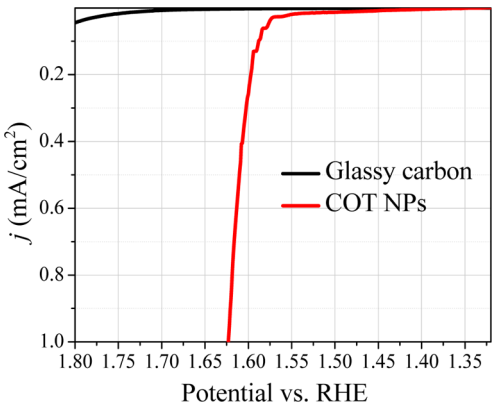

Figure 11. OER performance of COT NPs in 0.1 M O_2-saturated KOH analyzed from a RDE system. Loading of COT NPs is 0.1 mg/cm^2 on a glassy carbon electrode; rotation speed, 1600 rpm; scan rate, 10 mV/s.

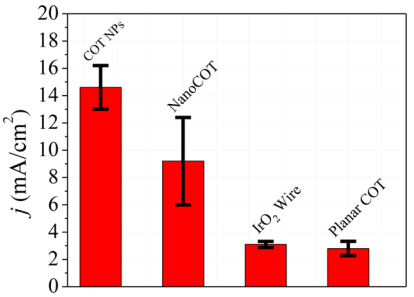

Figure 12. Average OER performances of COT NPs, NanoCOT, IrO_2, and planar COT at 1.77 V (vs RHE). The error bar represents the distribution of the measured current density from five independent measurements.

area that is higher than for other catalysts. The OER efficiency of NanoCOT is ∼2−4 times that of IrO_2, depending on the surface areas of the different substrates. In addition, the planar COT shows an efficiency close to that of the IrO_2 wire.

3.5. Water Reduction Performance of NanoCOT and Complete Water Electrolysis at NanoCOT Electrodes. A cathode is needed for complete water splitting, and Pt is always the best option for this because of favorable proton reduciton at its surface. Proton reduction is sluggish at the NanoCOT cathode, in contrast to Pt electrode, as shown by Figure S10. To overcome this issue, we electrochemically coated the

DOI: 10.1021/jacs.5b05367
J. Am. Chem. Soc. 2015, 137, 11996−12005

NanoCOT electrode with NiMoZn. Enhanced proton reduction efficiency at the NanoCOT can be achieved with a surface coating of NiMoZn, as shown in Figure S10. SEM and a photograph of the modified NanoCOT electrode with NiMnZn are shown in Figure S11. To demonstrate the enhanced water splitting capability of a NanoCOT anode, various combinations of anode and cathode electrodes, including Pt, NanoCOT, IrO_2 wire, and NiMoZn, were evaluated using linear scanning voltammetry for water splitting in 0.1 M KOH, as shown in Figure 13. The combination of NiMoZn/NanoCOT (cathode) and NanoCOT (anode) exhibited the highest current density of 99 mA/cm^2 at 3 V, which is higher than the 70 mA/cm^2 of IrO_2 and 26 mA/cm^2 of Pt. We have attempted to wire this pair of NanoCOT electrodes to a silicon solar cell whose potential output is set to 2.0 V by using a potentiometer wired to the solar cell panel to generate oxygen and hydrogen, as shown in the bottom inset of Figure 13.

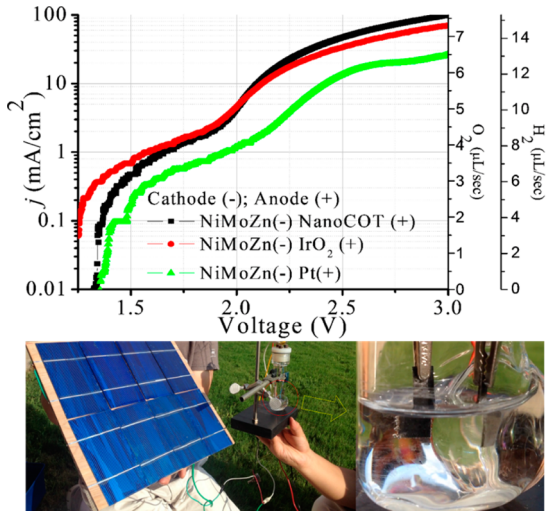

Figure 13. Linear scanning voltammetry curves and O_2/H_2 fluxes at standard temperature and pressure (STP) of three pairs of anode and cathode electrodes in 0.1 M KOH solution for complete water electrolysis at a scan rate of 5 mV/s. Bottom inset is the optimal combination of NiMoZn/NanoCOT (cathode) and NanoCOT (anode) electrode for complete water splitting at 2.0 V DC output provided by a 12.5% silicon solar cell panel wired to a potentiometer under sunlight outside Shelby Hall of the University of Alabama in Fall 2014.

3.6. Mechanism. We hypothesize that the NanoCOT surface is more active because the predominant reduced Ti (Ti^{1+}, Ti^{2+}, Ti^{3+}) defect states provide a high concentration of active sites for water absorption and dissociation, which is a critical first step in the process of OER. The rich and unusual valence states of Ti (Ti^{1+},Ti^{2+}, Ti^{3+}, and Ti^{4+}) that undergo hybridization with the C 2p and O 2p states in the NanoCOT electrode form a continuous energy band that plays an important role in enhancing carrier conductivity and active sites' performance, leading to a higher OER performance with a low overpotential. Furthermore, the direct growth of NanoCOT on the Ti substrate, which can efficiently collect and transfer electrons, enables strong bonding between NanoCOT and the Ti electrode, and thus, an enhanced OER stability is presumably another important reason for the enhanced OER performance. A computational study is being carried out to obtain an improved understanding of the NanoCOT's enhanced performance for OER. Such a carbon-modified titanium oxide electrode material could be achieved by oxidizing or anodizing TiC directly, although it is nontrivial to achieve the right composition with such a facile and economical method, as shown by our preliminary test result in Figures S12 and S13.

It should be noted that the residual Fe content in our NanoCOT is not responsible for the obtained OER activity. To assess the possible effect of residual Fe on the OER activity of the NanoCOT electrode, we have carried out four control experiments to conclusively demonstrate that the trace of Fe or Fe/C on the surface is not responsible for the high efficiency of the NanoCOT's OER. This includes the OER performance of (1) the NanoCOT electrode with Fe leached out using a strong acid (Figures S14 and S15); (2) a CVD-treated bare Fe plate with and without $Fe(NO_3)_3$ treatment (Figure S16); (3) a thermally annealed NanoCOT sample in air (Figure S17); and (4) a CVD-treated TiO_2 nanowire substrate without $Fe(NO_3)_3$ treatment (Figure S18). On the basis of all the above control investigations, we conclude that the residue amount of Fe is not responsible for the enhanced OER. We believe that the role of $Fe(NO_3)_3$ reduced by hydrogen in our CVD system is to help decompose CH_4 into carbon and hydrogen for TiO_2 reduction

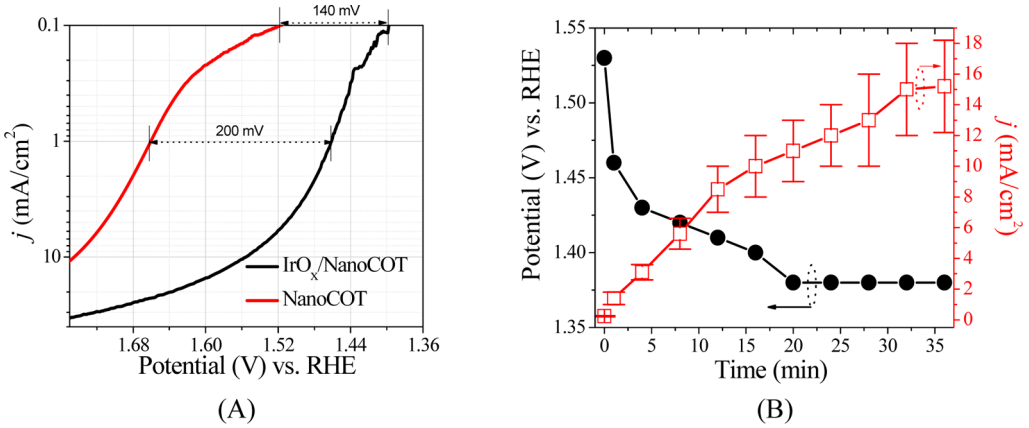

Figure 14. Polarization curves of 2 nm IrO_x NPs/NanoCOT (36 min deposition time) and NanoCOT electrode in 0.1 M KOH at 5 mV/s (A). Applied potential at current densities of 0.1 mA/cm^2 (black) and 1.6 V (vs RHE) (red) of 2 nm IrO_x nanoparticle-coated NanoCOT as a function of electrophoresis deposition time (B). The error bar represents the distribution of the measured current densities of four independent measurements.

DOI: 10.1021/jacs.5b05367
J. Am. Chem. Soc. 2015, 137, 11996−12005

and carbon doping, which is helpful for converting TiO_2 into the NanoCOT with high OER activity.

3.7. Enhanced OER Reaction at NanoCOT using IrO_x NPs. It is well-known that the electrochemical properties of Ir oxide with an undefined stoichiometry (IrO_x) are strongly dependent on the particle size. For example, 2 nm IrO_x exhibits a thermodynamically and kinetically favorable water oxidation capability with a minimum overpotential reported.[41,46] To compare the NanoCOT electrode with 2 nm IrO_x, the OER performance of the NanoCOT coated with 2 nm IrO_x NPs nanoparticles was studied. The amount of 2 nm IrO_x NPs on the NanoCOT can be controlled by the electrophoretic deposition time. The IrO_x NPs' coating thickness increases with deposition time. As shown in Figure 14A, a 36 min deposition of IrO_x onto the NanoCOT yields 140 mV less overpotential than an as-synthesized NanoCOT at a current density of 0.1 mA/cm^2. The NanoCOT's current density of 10.3 mA/cm^2 at 1.75 V (vs RHE) can be improved to 30 mA/cm^2 with a 36 min coating with IrO_x NPs. Figure 14B shows that the OER onset potential decreases with increasing loading of 2 nm IrO_x NPs onto NanoCOT, accompanied by an increase in its current density at 1.6 V (vs RHE). The OER performance of the IrO_x/NanoCOT electrode can be improved with a longer deposition time, and its onset potential can reach 1.38 V (vs RHE), which is equivalent to η = 150 mV for water oxidation, after 20 min, and the current density at 1.6 V vs RHE reaches as high as 15 mA/cm^2 at a deposition time of 32 min.

4. CONCLUSIONS

In summary, we present a low-cost NanoCOT electrode containing earth-abundant elements and operating efficiently in alkaline solution for OER with appreciable catalytic current of only ~300 mV overpotential. The NanoCOT is prepared by facile carbon thermal transformation of a nanostructured Ti substrate or TiO_2 NPs in an atmosphere of methane, hydrogen, and nitrogen. This catalytic performance for OER of NanoCOT can be further improved by coating its surface with 2 nm IrO_x NPs. With its lower cost and superior performance for OER over IrO_2 and Pt samples, NanoCOT holds the promise for being used as an active electrode material in an electrolyzer. On the basis of the evidence provided by surface structural analysis, we find predominant valence and defect states of Ti (Ti^{1+},Ti^{2+}, Ti^{3+}, and Ti^{4+}) and significant hybridization of the C 2p and O 2p states. Along with the intimate electrical contact between NanoCOT and the Ti substrate, NanoCOT can potentially benefit efficient water splitting and other electrochemical applications by replacing precious metals such as Pt or Ir. NanoCOT can be engineered to form COT NPs to enhance their current density of OER and applications of NanoCOT onto other electrical conductive substrates (e.g., glassy carbon, indium−tin oxide, and stainless steel).

■ ASSOCIATED CONTENT

Supporting Information

The Supporting Information is available free of charge on the ACS Publications website at DOI: 10.1021/jacs.5b05367.

Figures S1−S18 (PDF)

■ AUTHOR INFORMATION

Corresponding Author

*span1@ua.edu

Notes

The authors declare no competing financial interest.

■ ACKNOWLEDGMENTS

This work is supported by the National Science Foundation under Award No. CHE-1153120. We acknowledge valuable discussions with Professor Allen Bard and Professor Thomas Meyer. We acknowledge Steven Kelly for assisting with planar COT XRD measurement. We acknowledge The Central Analytical Facility (CAF) of The University of Alabama for its major research instrumentation support.

■ REFERENCES

(1) Yeo, B. S.; Bell, A. T. *J. Am. Chem. Soc.* **2011**, *133*, 5587−5593.
(2) Gasteiger, H. A.; Markovic, N. M. *Science* **2009**, *324*, 48−49.
(3) Walter, M. G.; Warren, E. L.; McKone, J. R.; Boettcher, S. W.; Mi, Q.; Santori, E. A.; Lewis, N. S. *Chem. Rev.* **2010**, *110*, 6446−6473.
(4) Cheng, F. Y.; Chen, J. *Chem. Soc. Rev.* **2012**, *41*, 2172−2192.
(5) Armand, M.; Tarascon, J. M. *Nature* **2008**, *451*, 652−657.
(6) Lu, Y. C.; Xu, Z. C.; Gasteiger, H. A.; Chen, S.; Hamad-Schifferli, K.; Shao-Horn, Y. J. *J. Am. Chem. Soc.* **2010**, *132*, 12170−12171.
(7) Winter, M.; Brodd, R. J. *Chem. Rev.* **2004**, *104*, 4245−4269.
(8) Gewirth, A. A.; Thorum, M. S. *Inorg. Chem.* **2010**, *49*, 3557−3566.
(9) Debe, M. K. *Nature* **2012**, *486*, 43.
(10) Suntivich, J.; Gasteiger, H. A.; Yabuuchi, N.; Nakanishi, H.; Goodenough, J. B.; Shao-Horn, Y. *Nat. Chem.* **2011**, *3*, 546−550.
(11) Devadoss, A.; Sudhagar, P.; Das, S.; Lee, S. Y.; Terashima, C.; Nakata, K.; Fujishima, A.; Choi, W. B.; Kang, Y. S.; Paik, U. *ACS Appl. Mater. Interfaces* **2014**, *6*, 4864−4871.
(12) Bing, Y.; Liu, H.; Zhang, L.; Ghosh, D.; Zhang, J. *Chem. Soc. Rev.* **2010**, *39*, 2184−2202.
(13) Gorlin, Y.; Jaramillo, T. F. *J. Am. Chem. Soc.* **2010**, *132*, 13612−13614.
(14) Lee, Y.; Suntivich, J.; May, K. J.; Perry, E. E.; Shao-Horn, Y. *J. Phys. Chem. Lett.* **2012**, *3*, 399−404.
(15) Gasteiger, H. A.; Kocha, S. S.; Sompalli, B.; Wagner, F. T. *Appl. Catal., B* **2005**, *56*, 9−35.
(16) Trasatti, S. *Electrochim. Acta* **1984**, *29*, 1503−1512.
(17) Ardizzone, S.; Fregonara, G.; Trasatti, S. *Electrochim. Acta* **1990**, *35*, 263−267.
(18) Nakagawa, T.; Beasley, C. A.; Murray, R. W. *J. Phys. Chem. C* **2009**, *113*, 12958−12961.
(19) Lee, Y. M.; Suntivich, J.; May, K. J.; Perry, E. E.; Shao-Horn, Y. *J. Phys. Chem. Lett.* **2012**, *3*, 399−404.
(20) Cormier, Z. R.; Andreas, H. A.; Zhang, P. *J. Phys. Chem. C* **2011**, *115*, 19117−19128.
(21) Kanan, M. W.; Nocera, D. G. *Science* **2008**, *321*, 1072−1075.
(22) Suntivich, J.; May, K. J.; Gasteiger, H. A.; Goodenough, J. B.; Shao-Horn, Y. *Science* **2011**, *334*, 1383−1385.
(23) Liang, Y. Y.; Li, Y. G.; Wang, H. L.; Zhou, J. G.; Wang, J.; Regier, T.; Dai, H. J. *Nat. Mater.* **2011**, *10*, 780−786.
(24) Zhao, Y.; Nakamura, R.; Kamiya, K.; Nakanishi, S.; Hashimoto, K. *Nat. Commun.* **2013**, *4*, 2390.
(25) Subbaraman, R.; Tripkovic, D.; Chang, K. C.; Strmcnik, D.; Paulikas, A. P.; Hirunsit, P.; Chan, M.; Greeley, J.; Stamenkovic, V.; Markovic, N. M. *Nat. Mater.* **2012**, *11*, 550−557.
(26) Li, Y. G.; Wang, H. L.; Xie, L. M.; Liang, Y. Y.; Hong, G. S.; Dai, H. J. *J. Am. Chem. Soc.* **2011**, *133*, 7296−7299.
(27) Gong, M.; Li, Y. G.; Wang, H. L.; Liang, Y. Y.; Wu, J. Z.; Zhou, J. G.; Wang, J.; Regier, T.; Wei, F.; Dai, H. J. *J. Am. Chem. Soc.* **2013**, *135*, 8452−8455.
(28) Wang, J.; Zhong, H. X.; Qin, Y. L.; Zhang, X. B. *Angew. Chem., Int. Ed.* **2013**, *52*, 5248−5253.
(29) Louie, M. W.; Bell, A. T. *J. Am. Chem. Soc.* **2013**, *135*, 12329−12337.
(30) Zou, X. X.; Goswami, A.; Asefa, T. *J. Am. Chem. Soc.* **2013**, *135*, 17242−17245.

DOI: 10.1021/jacs.5b05367
J. Am. Chem. Soc. 2015, 137, 11996−12005

(31) Trotochaud, L.; Ranney, J. K.; Williams, K. N.; Boettcher, S. W. *J. Am. Chem. Soc.* **2012**, *134*, 17253−17261.
(32) Gao, M. R.; Xu, Y. F.; Jiang, J.; Zheng, Y. R.; Yu, S. H. *J. Am. Chem. Soc.* **2012**, *134*, 2930−2933.
(33) Li, Y.; Hasin, P.; Wu, Y. Y. *Adv. Mater.* **2010**, *22*, 1926−1929.
(34) Meng, Y. T.; Song, W. Q.; Huang, H.; Ren, Z.; Chen, S. Y.; Suib, S. L. *J. Am. Chem. Soc.* **2014**, *136*, 11452−11464.
(35) Lee, D. U.; Kim, B. J.; Chen, Z. W. *J. Mater. Chem. A* **2013**, *1*, 4754−4762.
(36) Scheffe, J. R.; Li, J. H.; Weimer, A. W. *Int. J. Hydrogen Energy* **2010**, *35*, 3333−3340.
(37) Mole, F.; Wang, J.; Clayton, D. A.; Xu, C.; Pan, S. L. *Langmuir* **2012**, *28*, 10610−10619.
(38) Hahn, R.; Schmidt-Stein, F.; Salonen, J.; Thiemann, S.; Song, Y. Y.; Kunze, J.; Lehto, V. P.; Schmuki, P. *Angew. Chem., Int. Ed.* **2009**, *48*, 7236−7239.
(39) Huang, K.; Li, Y. F.; Xing, Y. *J. Mater. Res.* **2013**, *28*, 454−460.
(40) Shan, Z. C.; Clayton, D.; Pan, S. L.; Archana, P. S.; Gupta, A. J. *J. Phys. Chem. B* **2014**, *118*, 14037−14046.
(41) Oberson, P. G.; Ankem, S. *Int. J. Plast.* **2009**, *25*, 881−900.
(42) Nocera, D. G. *Acc. Chem. Res.* **2012**, *45*, 767−776.
(43) Nakagawa, T.; Beasley, A. C.; Murray, W. R. *J. Phys. Chem. C* **2009**, *113*, 12958−12961.
(44) Xu, C. L.; Geng, H. W.; Bennett, R.; Clayton, D. A.; Pan, S. L. *J. Phys. Chem. C* **2013**, *117*, 1849−1856.
(45) Cheng, F. Y.; Shen, J.; Peng, B.; Pan, Y. D.; Tao, Z. L.; Chen, J. *Nat. Chem.* **2011**, *3*, 79−84.
(46) Tilley, S. D.; Cornuz, M.; Sivula, K.; Grätzel, M. *Angew. Chem., Int. Ed.* **2010**, *49*, 6405−6408.

DOI: 10.1021/jacs.5b05367
J. Am. Chem. Soc. 2015, 137, 11996−12005